The Astrophysical Journal, 621:41–52, 2005 March 1

THE CLUSTERING OF EXTRAGALACTIC EXTREMELY RED OBJECTS

Michael J. I. Brown,[1,2] Buell T. Jannuzi,[2] Arjun Dey,[2] and Glenn P. Tiede[3]

Received 2004 August 20; accepted 2004 November 15

ABSTRACT

We have measured the angular and spatial clustering of 671 $K < 18.40$, $R - K > 5$ extremely red objects (EROs) from a 0.98 deg^2 subregion of the NOAO Deep Wide-Field Survey (NDWFS). Our study covers nearly 5 times the area and has twice the sample size of any previous ERO clustering study. The wide field of view and $B_W RIK$ passbands of the NDWFS allow us to place improved constraints on the clustering of $z \sim 1$ EROs. We find that the angular clustering of EROs is slightly weaker than in previous measurements, and $\omega(1') = 0.25 \pm 0.05$ for $K < 18.40$ EROs. We find no significant correlation of ERO spatial clustering with redshift, apparent color, or absolute magnitude, although given the uncertainties, such correlations remain plausible. We find that the spatial clustering of $K < 18.40$, $R - K > 5$ EROs is well approximated by a power law, with $r_0 = 9.7 \pm 1.1\ h^{-1}$ Mpc in comoving coordinates. This is comparable to the clustering of $\sim 4L^*$ early-type galaxies at $z < 1$ and is consistent with the brightest EROs being the progenitors of the most massive elliptical galaxies. There is evidence of the angular clustering of EROs decreasing with increasing apparent magnitude, when NDWFS measurements of ERO clustering are combined with those from the literature. Unless the redshift distribution of $K \gtrsim 20$ EROs is very broad, the spatial clustering of EROs decreases from $r_0 = 9.7 \pm 1.1\ h^{-1}$ Mpc for $K < 18.40$ to $r_0 \sim 7.5\ h^{-1}$ Mpc for $K \gtrsim 20$ EROs.

Subject headings: cosmology: observations — galaxies: elliptical and lenticular, cD — galaxies: high-redshift — large-scale structure of universe

Online material: color figures

1. INTRODUCTION

The evolution of galaxy clustering is a prediction of hierarchical models of galaxy and structure formation (e.g., Kauffmann et al. 1999; Benson et al. 2001; Somerville et al. 2001). Hierarchical models for a concordance cosmology[4] predict little or no evolution of the clustering of $\gtrsim L^*$ red galaxies at $z < 2$. Precise measurements of galaxy clustering at $z \sim 1$ can therefore test the predictions of these models.

Extremely red objects (EROs; Elston et al. 1988; McCarthy et al. 1992; Hu & Ridgway 1994; Dey et al. 1995) could be the progenitors of local elliptical galaxies (e.g., Spinrad et al. 1997). Roughly 80% of $K_S < 18.7$ EROs have spectra with the absorption features of old stellar populations (Yan et al. 2004), and $\sim$50% of $K \lesssim 22$ EROs have early-type morphologies (Moriondo et al. 2000; Stiavelli & Treu 2001; Moustakas et al. 2004). Some EROs contain supermassive black holes, since $\sim$15% of EROs contain an obscured active galactic nucleus that can be detected by deep X-ray surveys (Alexander et al. 2002; Roche et al. 2003). A direct test of the relationship between $z \sim 1$ EROs and the most massive local elliptical galaxies is to compare the spatial clustering of the two populations.

Previous constraints on the spatial correlation function of EROs, summarized in Table 1, are provided by pencil beam surveys with $\lesssim 0.2$ deg^2 areal coverage each. Individual structures composed of EROs can have sizes comparable to the field of view of these surveys (e.g., Daddi et al. 2000), and small surveys do not sample representative volumes of the universe for highly clustered objects (e.g., Somerville et al. 2004). At $z \sim 1$, the transverse comoving distance spanned by previous ERO studies is $\lesssim 20\ h^{-1}$ Mpc, which is much smaller than the size of individual structures observed in the present-day universe. Spatial clustering measurements derived from the angular correlation function depend on ERO redshift distribution models. Previous angular clustering studies were unable to verify their model redshift distributions, as complete spectroscopic samples of EROs were unavailable. Previous ERO spatial clustering measurements have large uncertainties and possibly large (and sometimes unaccounted for) systematic errors.

In this paper, we present a measurement of the clustering of EROs using $B_W RIK$ imaging of a 0.98 deg^2 subset of the NOAO Deep Wide-Field Survey (NDWFS). The large area of our study provides a more representative volume than previous studies. The $B_W RIK$ passbands of the NDWFS allow us to constrain the ERO redshift distribution with photometric redshifts and their uncertainties. We also use photometric redshifts to select EROs as a function of luminosity and redshift. We use ERO spectroscopic redshifts to verify the accuracy of our photometric redshifts, and we compare our estimate of the ERO redshift distribution with spectroscopic redshift distributions from the literature.

The structure of the paper is as follows. In § 2 we provide a brief description of the NDWFS imaging and catalogs from which the $K < 18.40$ ERO sample was selected. We discuss our estimates of ERO photometric redshifts and provide a comparison of ERO photometric and spectroscopic redshifts in § 3. The selection of the ERO sample and ERO number counts are discussed in § 4. In § 5, we describe the techniques used to measure the angular and spatial correlation functions. The angular and spatial clustering of EROs as a function of apparent

[1] Princeton University Observatory, Peyton Hall, Princeton, NJ 08544-1001; mbrown@astro.princeton.edu.

[2] National Optical Astronomy Observatory, P.O. Box 26732, Tucson, AZ 85726-6732; jannuzi@noao.edu, dey@noao.edu.

[3] Department of Physics and Astronomy, Bowling Green State University, Bowling Green, OH 43403; gptiede@bgnet.bgsu.edu.

[4] Throughout this paper $H_0 \equiv 100\ h$ km s^{-1} Mpc^{-1}, $\Omega_m = 0.3$, $\Lambda = 0.7$, and comoving coordinates.

TABLE 1

SUMMARY OF ERO SPATIAL CLUSTERING STUDIES

Survey[a]	Area (arcmin^2)	Number of Galaxies	Magnitude Range	Selection	Additional Selection Criteria	Measured or Model z Range	z Distribution Model[b]	r_0 Comoving[c] (h^{-1} Mpc)	Assumed Value of γ[d]
NDWFS.....	3529	671	$K < 18.40$	$R - K > 5$	...	$0.8 \lesssim z \lesssim 3.0$	PhotZ	9.7 ± 1.0	1.87
K20.....	52	18	$K < 19.2$	$R - K > 5$	Dusty SF SED	$0.796 \leq z \leq 1.419$	Spectra	$\lesssim 2.5$	1.8
K20.....	52	15	$K < 19.2$	$R - K > 5$	Old stellar SED	$0.726 \leq z \leq 1.222$	Spectra	5.5–16	1.8
NTT-WHT.....	701	400	$K < 19.2$	$R - K > 5$	...	$0.8 \lesssim z \lesssim 2.0$	PE	13.8 ± 1.5	1.8
LCIRS	744	337	$H < 20.0$	$R - H > 4$	...	$0.7 \lesssim z \lesssim 1.5$	PhotZ	11.1 ± 2.0	1.8
LCIRS	407	312	$H < 20.5$	$R - H > 4$	...	$0.7 \lesssim z \lesssim 1.5$	PhotZ	7.7 ± 2.4	1.8
Subaru	114	134	$K < 20.2$	$R - K_S > 5$	Dusty SF SED	$0.0 < z < 4.3$	PhotZ	12 ± 2	1.8
Subaru	114	143	$K < 20.2$	$R - K_S > 5$	Old stellar SED	$0.0 < z < 4.3$	PhotZ	11 ± 1	1.8
ELAIS N2.....	81.5	158	$K < 20.25$	$R - K > 5$	...	$1 \lesssim z \lesssim 3$	M-DE	12.8 ± 1.5	1.8
ELAIS N2.....	81.5	158	$K < 20.25$	$R - K > 5$	...	$1 \lesssim z \lesssim 3$	NE	10.3 ± 1.2	1.8
CDF-S	50.4	198	$K_S < 22.0$	$I_{775} - K_S > 3.92$	...	$1 \lesssim z \lesssim 3$	M-DE	12.5 ± 1.2	1.8
HDF-S.....	4	18	$K < 24.0$	$I - K > 4$	...	...	PhotZ	$16.9^{+2.9}_{-5.5}$	1.8
HDF-S.....	4	39	$K < 24.0$	$I - K > 3.5$	...	...	PhotZ	$6.2^{+5.4}_{-7.1}$	1.8
HDF-S.....	4	23	$K < 24.0$	$I - K > 3.5$	$0.8 < z < 2.0$	$0.8 \lesssim z \lesssim 2.0$	PhotZ	9.7 ± 2.0	1.8

[a] CDF-S (Chandra Deep Field–South): Roche et al. (2003); ELAIS N2: Roche et al. (2002); HDF-S: Daddi et al. (2003); NTT-WHT: Daddi et al. (2001); K20: Daddi et al. (2002); LCIRS: Firth et al. (2002); Subaru: Miyazaki et al. (2003).

[b] M-DE = merging and density evolution (Roche et al. 2002); NE = no evolution (Roche et al. 2002); PE = single burst and passive evolution (Daddi et al. 2001); PhotZ = photometric redshifts (Firth et al. 2002; Daddi et al. 2003; Miyazaki et al. 2003; this work).

[c] Values of r_0 are for a $\Omega_m = 0.3$, $\Lambda = 0.7$ cosmology. Uncertainties are as published, and were determined using a variety of techniques.

[d] For this study, changing the value of γ from 1.87 to 1.80 increases r_0 by $\simeq$10%.

magnitude, apparent color, absolute magnitude, and redshift are discussed in § 6. We discuss the implications of our results in § 7 and summarize the paper in § 8.

2. THE NOAO DEEP WIDE-FIELD SURVEY

The NDWFS is a multiband (B_W, R, I, K) survey of two $\approx$9.3 deg^2 high Galactic latitude fields with the Cerro Tololo Inter-American Observatory (CTIO) 4 m, Kitt Peak National Observatory (KPNO) 4 m, and KPNO 2.1 m telescopes (Jannuzi & Dey 1999). A thorough description of the optical and K-band observing strategy and data reduction will be provided by B. T. Jannuzi et al. (2005, in preparation) and A. Dey et al. (2005, in preparation). This paper utilizes 0.98 deg^2 of $B_W RIK$ data in the Boötes field. $B_W RI$ imaging and catalogs for the entire NDWFS Boötes field became available from the NOAO Science Archive[5] on 2004 October 22. K-band imaging and catalogs for approximately one-half the Boötes field are also available from this archive.

We generated object catalogs using SExtractor 2.3.2 (Bertin & Arnouts 1996), run in single-image mode in a manner similar to that of Brown et al. (2003). At faint magnitudes, detections in the different bands were matched if the centroids were within 1″ of each other. At bright magnitudes, detections in the different bands were matched if the centroids were within an ellipse defined using the second-order moments of the light distribution of the object.[6] Throughout this paper we use SExtractor MAG_AUTO magnitudes (which are similar to Kron total magnitudes; Kron 1980), because of their small uncertainties and systematic errors at faint magnitudes. Our clustering measurements are not particularly sensitive to how we measure ERO photometry, and the clustering of EROs selected with 4″ diameter aperture photometry is only marginally weaker than the clustering of EROs selected with MAG_AUTO photometry.

We determined the completeness as a function of magnitude by adding artificial objects to copies of the data and recovering them with SExtractor. To approximate $z \sim 1$ galaxies, the artificial objects have an intrinsic profile with a full width at half-maximum of 0.″5, which was then convolved with a Moffat profile model of the seeing. The 50% completeness limits vary within the sample area in the ranges of $26.0 < B_W < 26.7$, $24.8 < R < 25.6$, $23.6 < I < 25.2$, and $18.6 < K < 18.7$.[7]

Regions surrounding saturated stars were removed from the catalog to exclude (clustered) spurious objects detected in the wings of the point-spread function. We excluded regions where the rms of the sky noise in the K-band data was 20% higher than the mean, since the depth of these regions is significantly less than the mean depth across the field. While it is plausible that smaller variations in the sky noise could alter the measured clustering of the faintest EROs, our main conclusions remain unchanged if we exclude $K > 18.15$ EROs from the sample.

We used SExtractor's star-galaxy classifier to remove objects from the galaxy catalog that had a stellarity of greater than 0.7 in two or more bands brighter than $B_W < 23.8$, $R < 22.8$, and $I < 21.4$. At fainter magnitudes we do not use the star-galaxy classification and correct the angular correlation function for the estimated stellar contamination of the sample. We do not use the K band for star-galaxy classification, since there are image quality variations across the K-band image stacks. We estimated stellar contamination of the galaxy sample using the same technique as Brown et al. (2003), in which the stellar number counts were assumed to be a power law and the distribution of stellar colors does not change with magnitude at $R \gtrsim 21$. The contamination of the ERO sample (§ 4) by stars is estimated to be $\sim$2%, and the conclusions of this paper remain unaltered unless stellar contamination is higher than 15%.

3. PHOTOMETRIC REDSHIFTS

Photometric redshifts were determined for all objects with I- and K-band detections. We provide a brief overview of the photometric redshifts here and refer the reader to our earlier study of $0.3 < z < 0.9$ red galaxy clustering in the NDWFS (Brown et al. 2003) for a more detailed description of the photometric redshift code. To model galaxy spectral energy distributions (SEDs), we used PEGASE2 evolutionary synthesis models (Fioc & Rocca-Volmerange 1997) with exponentially declining star formation rates (τ models) and $z = 0$ ages of 12 Gyr (formation $z \approx 4$). The effect of $E(B - V) = 0.04$ dust reddening with $R_V = 3.1$, comparable to estimates for $0 < z < 1$ early-type galaxies (Falco et al. 1999), was included in the τ-models. In Brown et al. (2003), we used models with solar metallicity at $z = 0$, which resulted in small systematic underestimates of galaxy redshifts. Simple solar metallicity τ-models underestimate the UV luminosity of galaxies (e.g., Donas et al. 1995), so in this work we let the metallicity of the models be a function of τ. This has the effect of slightly increasing the UV flux of the model SEDs. We verified the accuracy of the photometric redshifts at $z < 1$ with 89 $M_R < -19 - 5 \log h$ galaxies with rest-frame $B_W - R > 1.05$ and spectroscopic redshifts. After decreasing the metallicity of the models, the photometric redshifts of these red galaxies did not have significant systematic errors. We note, however, that the UV flux in galaxies can also be increased by the presence of young stars or by altering the properties of the dust extinction; our approach is merely a proxy for correcting any systematic effects in our photometric redshifts and is not meant to be interpreted as justifying subsolar metallicities in the red galaxy population. We use these solar and subsolar τ-models throughout the remainder of the paper. Color tracks for two of the models are shown in Figure 1. For comparison, we also show two ultraluminous infrared galaxy (ULIRG) templates from Devriendt et al. (1999), which have bluer $B_W - R$ colors than the τ-models at $z \sim 1$.

Photometric redshifts were estimated by finding the minimum value of χ^2 as a function of redshift, spectral type (τ), and luminosity. For objects not detected in the R or B_W bands, we estimated the probability of a nondetection using the completeness estimates discussed in § 2. Since the model SEDs do not account for the observed width of the galaxy locus, we increased the photometric uncertainties for the galaxies by 0.05 mag (added in quadrature). To improve the accuracy of the photometric redshifts, the estimated redshift distribution of galaxies as a function of spectral type and apparent magnitude was introduced as a prior. The Two-Degree Field Galaxy Redshift Survey (2dFGRS) luminosity functions for different spectral types (Madgwick et al. 2002), with spectral evolution given by the τ-models, were used to estimate the redshift distributions.

We tested the reliability of the photometric redshifts with simulated galaxies and real galaxies with spectroscopic redshifts. Simulated galaxies were generated using the PEGASE2 τ-models. The simulated data consisted of $K < 18.40$ galaxies with 0.6 Gyr $\leq \tau \leq$ 15 Gyr in the redshift range $0 < z \leq 5$ and luminosity range $0.01 < L^* \leq 100$. The simulated object photometry was scattered using the estimated uncertainties, thus mimicking what would be present in the real catalogs.

[5] See http://www.archive.noao.edu/ndwfs.

[6] This ellipse was defined with the SExtractor parameters 2 × AWORLD, 2 × BWORLD, and THETAWORLD.

[7] Throughout this paper we use Vega photometry.

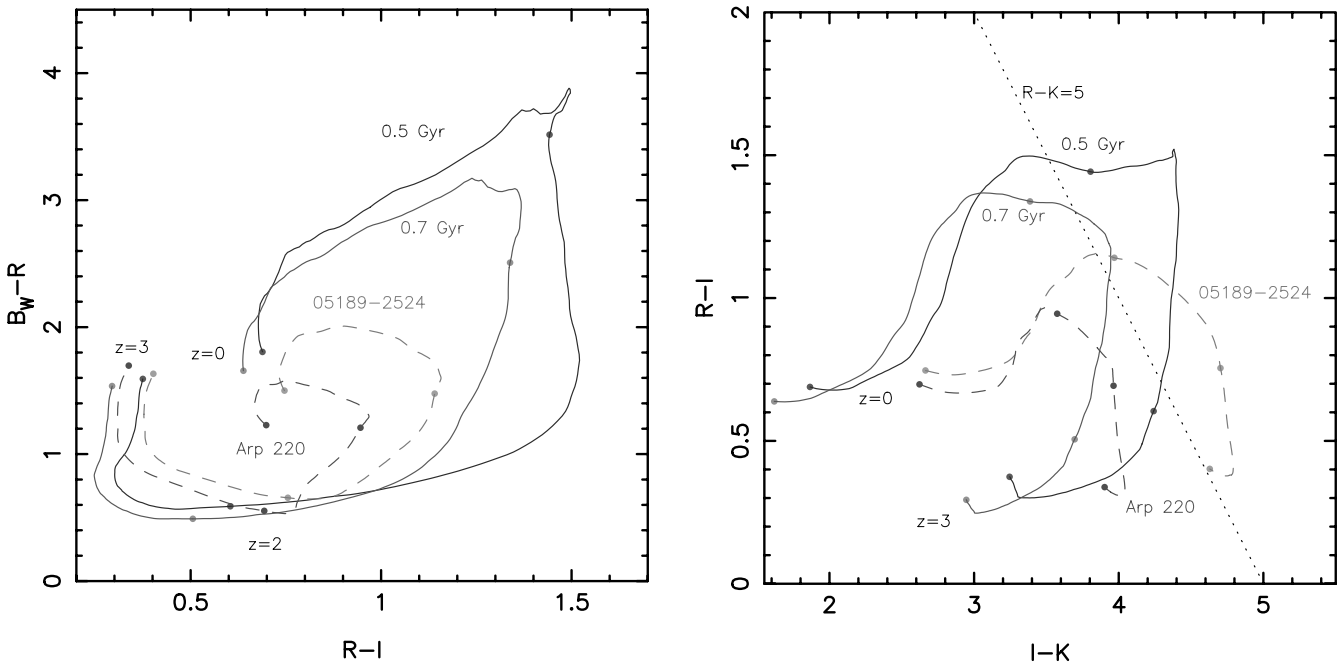

FIG. 1.—Color-color diagrams of the PEGASE2 τ-models and nonevolving templates of Arp 220 and IRAS 05189−2524 (Devriendt et al. 1999). The $R - K = 5$ selection criterion for EROs is shown (*right*). Dots mark $z = 0$, 1, 2, and 3 on the model tracks. For clarity, the redshift range shown is restricted to $0 \leq z \leq 3$ and we have not plotted τ-models bluer than the ERO color cut. [*See the electronic edition of the Journal for a color version of this figure.*]

We tested the accuracy of the photometric redshifts with a few spectroscopic redshifts and $B_W RIK$ photometry for EROs in the NDWFS Boötes field.

A comparison of our photometric and spectroscopic redshifts for EROs is shown in Figure 2. We discuss the selection criteria for the EROs in § 4. The simulated galaxies in Figure 2 (*left*) have 1 σ uncertainties of $\simeq$8%. For galaxies with SEDs similar to the PEGASE2 τ-models, our procedure should yield accurate photometric redshifts. There are four NDWFS $K < 18.40$ EROs with spectroscopic redshifts. As shown in Figure 2 (*right*), real EROs in the NDWFS exhibit a 1 σ scatter of $\sim$20% between the photometric and spectroscopic redshifts. There are more outliers than would be expected if the τ-models reproduced the variety of ERO SEDs. For comparison, GOODS obtains ERO photometric redshifts with accuracies of $\sim$5% (Mobasher et al. 2004), as they have photometry and upper limits in more bands

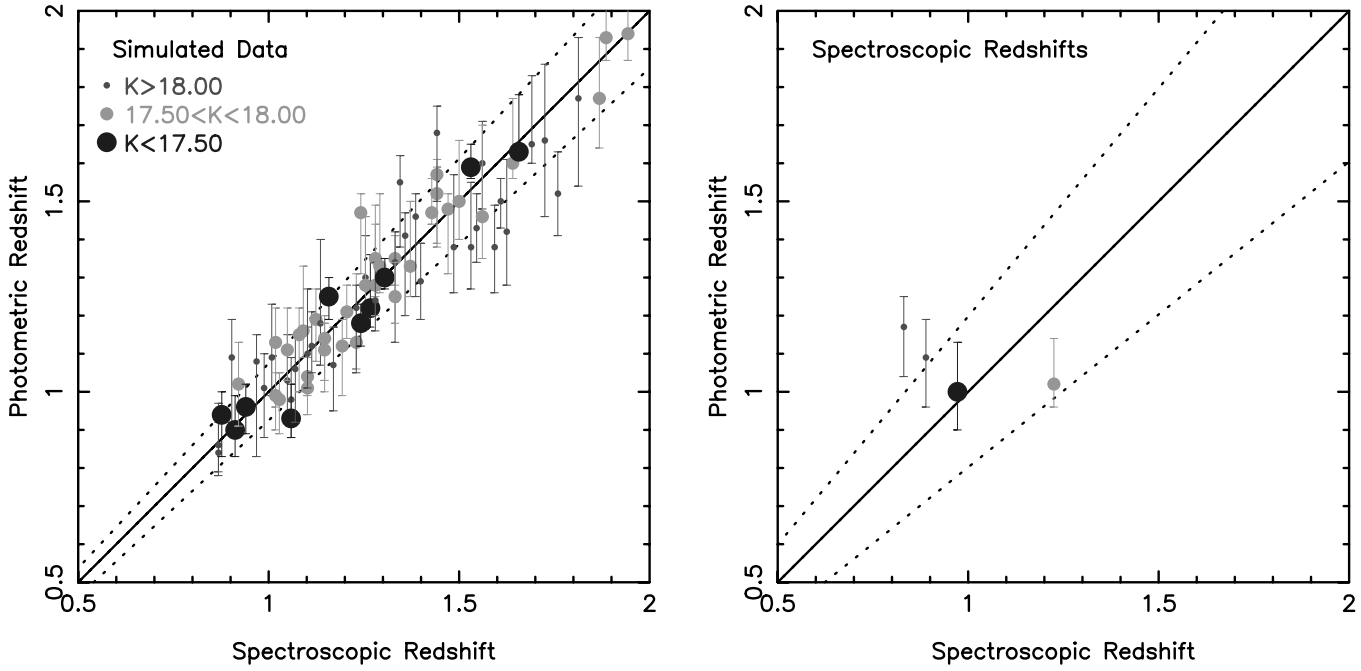

FIG. 2.—Comparison of $K < 18.40$, $R - K > 5.0$ ERO photometric and spectroscopic redshifts for simulated and real data. Dotted diagonal lines show the measured ± 1 σ uncertainties of the photometric redshifts. *Left:* Simulated EROs, generated using the τ-models with photometric noise added. *Right:* Real EROs with spectroscopic redshifts. For clarity only one-third of the simulated galaxies are plotted. The measured 1 σ uncertainties of the photometric redshifts for real EROs are $\sim$20%. [*See the electronic edition of the Journal for a color version of this figure.*]

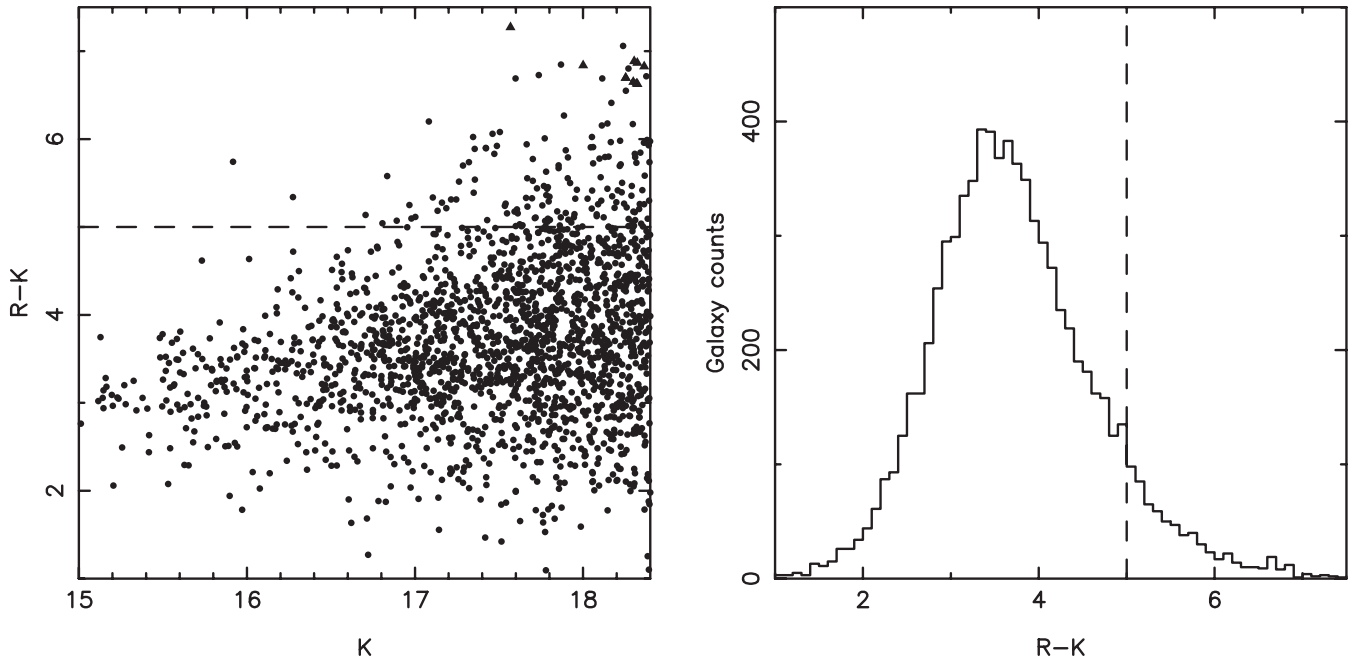

FIG. 3.—Color-magnitude diagram and number of $K < 18.40$ galaxies as a function of $R - K$ color. The $R - K = 5$ selection criterion is marked with dashed lines. Only 25% of all the galaxies have been plotted in the color-magnitude diagram, and $R - K$ lower limits are denoted by triangles. The R magnitude limits vary across the 0.98 deg^2 subregion, as the R-band imaging consists of four pointings. The uncertainty of the galaxy colors increases from $\simeq$0.1 mag at $K = 17.00$ to $\simeq$0.25 mag at $K = 18.40$. $R - K > 5.0$ EROs comprise $\simeq$8% of all $K < 18.4$ galaxies.

($U'UBB_{435}VV_{606}RIi_{775}z_{850}JHK_S$). The accuracy of photometric redshifts is a complex function of redshift, SED, and apparent magnitude. The accuracy of the ERO photometric redshifts could not be extrapolated from $z < 1$ red galaxy photometric redshifts, which can have uncertainties of less than 10% (e.g., Brown et al. 2003). The accuracy of ERO photometric redshifts cannot, and should not, be extrapolated from other samples of galaxies, such as samples selected by apparent magnitude only or from the Hubble Deep Fields (HDFs). Although our ERO photometric redshifts can only be considered approximations, they provide a good estimate of the ERO redshift distribution (see § 5).

4. THE EXTREMELY RED OBJECT SAMPLE

We selected EROs with the $R - K > 5$ criterion (e.g., Elston et al. 1988; Daddi et al. 2000; Roche et al. 2002), although redder color cuts are sometimes used in the literature (e.g., Hu & Ridgway 1994; Dey et al. 1999). We have limited the sample to $K < 18.40$ EROs to reduce the effects of completeness variations across the survey area on the measured clustering. As shown in Figure 3, the percentage of EROs increases from $\simeq$0% of the total galaxy counts at $K < 16$ to $\simeq$8% at $K \simeq 18.4$.

Contamination of the ERO sample by other galaxies could significantly alter the measured correlation function. At the magnitude limit of our sample, the uncertainty in the $R - K$ color is $\simeq$0.25 mag. For the distribution of galaxy colors shown in Figure 3, and assuming Gaussian photometric uncertainties, approximately 6% of the $K < 18.40$ ERO sample is contamination by $R - K < 4.75$ galaxies. Even if $R - K < 4.75$ galaxies were completely (and implausibly) unclustered, the amplitude of the $R - K > 5$ angular correlation function would only be decreased by 12%. Contamination by $4.75 < R - K < 5.00$ galaxies could be as high as 22% in the $K < 18.40$ ERO sample. This would significantly alter our results if the clustering of galaxies is a very strong function of color at $R - K \sim 5$. However, as discussed in § 6.2, we do not see evidence of this within our data set. Malmquist (1920) bias does increase the observed number of EROs. If we assume that the ERO number counts in Table 2 are a good approximation of the true ERO number counts, then the contribution of Malmquist bias to the NDWFS counts is $\lesssim$8%. This would alter the measured clustering if ERO angular clustering is an extremely strong function of apparent magnitude.

We assume that the bulk of our sample consists of galaxies with red stellar populations. The colors of dusty starbursts are predicted to differ significantly from galaxies with red stellar populations. As shown in Figure 4, 77% of the NDWFS ERO sample has $R - I > 1.15$, which is redder than the Devriendt et al. (1999) nonevolving ULIRG templates shown in Figure 1. Our assumption that most $K < 18.40$ EROs have red stellar populations is also consistent with the conclusions of Yan et al. (2004), who find that 86% of $K_S < 18.7$ EROs have the absorption features of old stellar populations.

The final sample consists of 671 objects, of which 318 are detected in the B_W band and 635 are detected in the R band. The $K < 18.4$ EROs have photometric redshifts in the range $0.8 \leq z \leq 3.0$, with the median of the distribution at $z \simeq 1.18$. Only five of the 671 $K < 18.4$ EROs have photometric redshifts of $z > 2$. ERO number counts as a function of K-band limiting magnitude are provided in Table 2 and Figure 5, along with results from previous surveys. We evaluated the uncertainties of the sky surface density for the NDWFS and previous work using the method discussed by Efstathiou et al. (1991), which includes the contribution of large-scale structure. The contribution of clustering to the uncertainties is typically several times larger than uncertainties determined by Poisson statistics. For our $K < 18.4$ ERO sample, accounting for the clustering increases the 1 σ uncertainty from 5% to 20%! We note that the uncertainties quoted by some studies do not include this contribution (e.g., Roche et al. 2002, 2003; Miyazaki et al. 2003). The distribution of the ERO sample on the plane of the sky is shown in Figure 6. ERO surveys of $\sim$0.1 deg^2 often have

TABLE 2

A Summary of ERO Angular Clustering Studies Including Number Counts and Sky Surface Density

Survey[a]	Area (arcmin^2)	Number of EROs	EROs per deg^2 [b]	Magnitude Range	Selection	$\omega(1')$[c]	Assumed γ-Value
This Study							
NDWFS.....	3529	256	$2.6 \pm 0.4 \times 10^2$	$K < 17.90$	$R - K > 5.0$	0.36 ± 0.13	1.87
NDWFS.....	3529	421	$4.3 \pm 0.6 \times 10^2$	$K < 18.15$	$R - K > 5.0$	0.23 ± 0.07	1.87
NDWFS.....	3529	671	$6.8 \pm 0.9 \times 10^2$	$K < 18.40$	$R - K > 5.0$	0.25 ± 0.05	1.87
Previous Studies Ordered by Limiting Magnitude							
NTT-WHT.....	701	58	$2.9 \pm 1.0 \times 10^2$	$K_S < 18.00$	$R - K_S > 5.0$	0.63 ± 0.26	1.8
NTT-WHT.....	701	106	$5.4 \pm 1.8 \times 10^2$	$K_S < 18.25$	$R - K_S > 5.0$	0.66 ± 0.13	1.8
NTT-WHT.....	701	158	$8.1 \pm 2.5 \times 10^2$	$K_S < 18.40$	$R - K_S > 5.0$	0.58 ± 0.08	1.8
NTT-WHT.....	701	279	$1.4 \pm 0.4 \times 10^3$	$K_S < 18.80$	$R - K_S > 5.0$	0.37 ± 0.05	1.8
LCIRS	744	337	$1.6 \pm 0.4 \times 10^3$	$H < 20.0$	$R - H > 4.0$	0.33 ± 0.11	1.8
LCIRS	744	201	$9.7 \pm 2.4 \times 10^2$	$H < 20.0$	$I - H > 3.0$	0.36 ± 0.18	1.8
NTT-WHT.....	447.5	281	$2.3 \pm 0.6 \times 10^3$	$K_S < 19.20$	$R - K_S > 5.0$	0.34 ± 0.04	1.8
Subaru	114	111	$3.5 \pm 1.1 \times 10^3$	$K_S < 19.2$	$R - K_S > 5.0$	0.29 ± 0.05	1.8
LCIRS	407	312	$2.8 \pm 0.5 \times 10^3$	$H < 20.5$	$R - H > 4.0$	0.17 ± 0.09	1.8
LCIRS	407	170	$1.5 \pm 0.3 \times 10^3$	$H < 20.5$	$I - H > 3.0$	0.20 ± 0.16	1.8
ELAIS N2	81.5	73	$3.2 \pm 1.3 \times 10^3$	$K < 19.50$	$R - K > 5.0$	0.40 ± 0.16	1.8
ELAIS N2	81.5	93	$4.1 \pm 1.3 \times 10^3$	$K < 19.75$	$R - K > 5.0$	0.23 ± 0.09	1.8
ELAIS N2	81.5	112	$4.9 \pm 1.4 \times 10^3$	$K < 20.00$	$R - K > 5.0$	0.20 ± 0.09	1.8
ELAIS N2	38.7	63	$5.9 \pm 1.5 \times 10^3$	$K < 20.25$	$R - K > 5.0$	0.10 ± 0.06	1.8
CDF-S	50.4	137	$9.8 \pm 2.6 \times 10^3$	$K_S < 21.00$	$I_{775} - K_S > 3.92$	0.14 ± 0.05	1.8
CDF-S	50.4	179	$1.3 \pm 0.4 \times 10^4$	$K_S < 21.50$	$I_{775} - K_S > 3.92$	0.16 ± 0.05	1.8
CDF-S	50.4	198	$1.4 \pm 0.4 \times 10^4$	$K_S < 22.00$	$I_{775} - K_S > 3.92$	0.13 ± 0.04	1.8
HDF-S	4	18	$1.6 \pm 0.8 \times 10^4$	$K < 24.00$	$I - K > 4$	0.16 ± 0.10	1.8

[a] CDF-S: Roche et al. (2003); ELAIS N2: Roche et al. (2002); HDF-S: Daddi et al. (2003); NTT-WHT: Daddi et al. (2000); LCIRS: Firth et al. (2002); Subaru: Miyazaki et al. (2003).

[b] The sky surface density has not corrected for the contribution of Malmquist bias. The 1 σ uncertainties assume Gaussian errors and include the contribution of the integral constraint (using the methodology of Efstathiou et al. 1991).

[c] Uncertainties for $\omega(1')$ are as published and may not include the effect of the covariance on the uncertainty estimates.

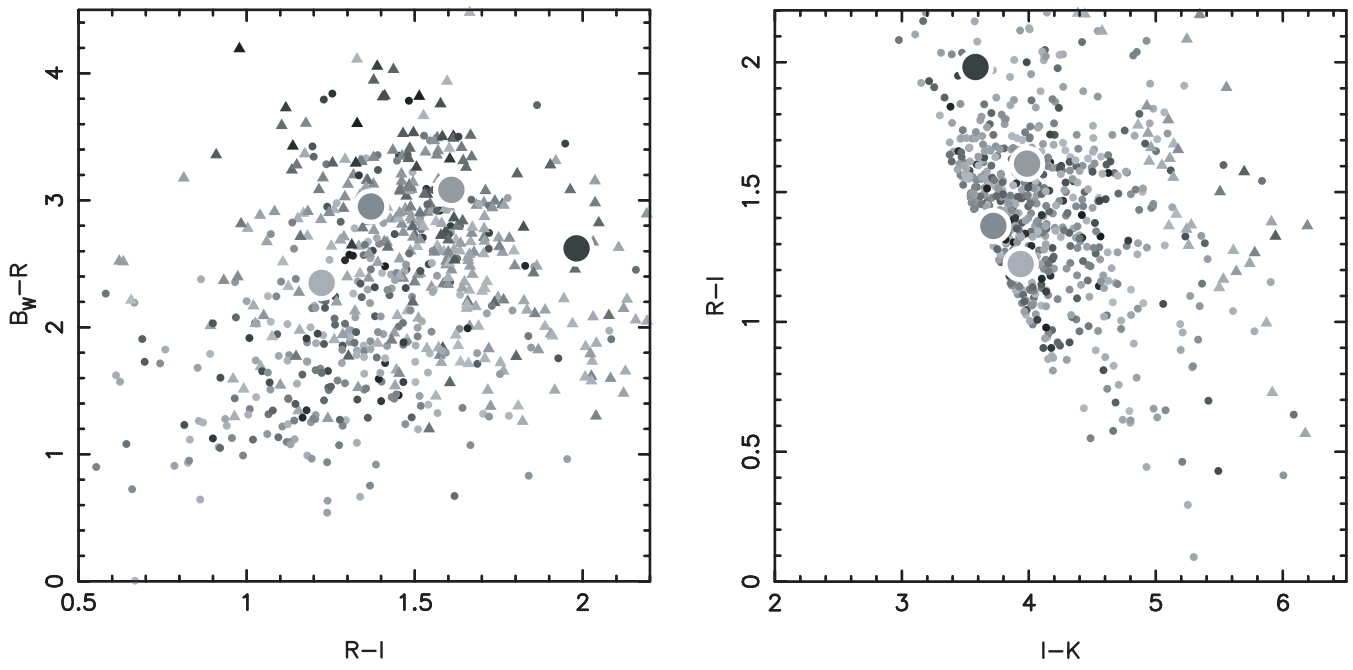

Fig. 4.—Color-color diagrams of the NDWFS ERO sample. B_W (*left*) and R (*right*) nondetections are shown with triangles, and large symbols denote EROs with spectroscopic redshifts. Black symbols are $K = 17$ or brighter, while paler symbols are fainter. The $B_W - R$ colors of most $K < 18.40$ EROs are redder than the ULIRG templates plotted in Fig. 1. A broad locus of galaxies can be seen at $R - I \sim 1.5$, which is coincident with the reddest PEGASE2 τ-models at $1.0 < z < 1.6$. The faintest objects in the sample have photometric uncertainties of $\sim$0.25 mag, so some objects with very unusual colors may be photometric errors.

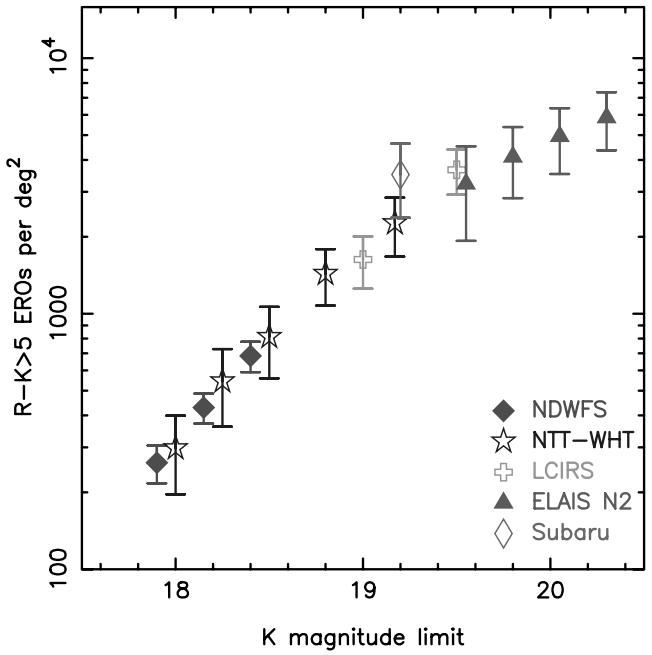

FIG. 5.—Cumulative sky surface density of $R - K > 5$ EROs as a function of K-band magnitude limit. LCIRS $R - H > 4$ EROs have been included using the assumption $H - K = 1$. References for each survey are listed in Table 1. We have estimated the uncertainties for each study using the integral constraint and the assumption of square fields of view. The sky surface densities of EROs measured by the different surveys are in good agreement. [*See the electronic edition of the Journal for a color version of this figure.*]

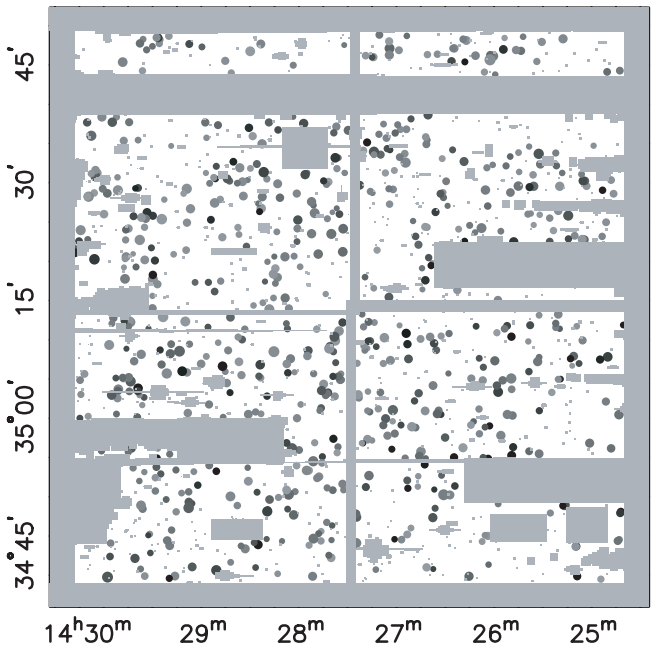

FIG. 6.—Distribution of NDWFS EROs on the plane of the sky. EROs are shown with dots, where the gray scale is a function of apparent magnitude (black dots are $K < 17$) while dot size is inversely proportional to the photometric redshift. Masked regions, such as subfield boundaries, saturated stars, and nonphotometric K-band data, are shown with gray rectangles. Clustering is evident in the plot, but there are no large gradients comparable to the sample area.

individual structures with sizes comparable to the field of view (e.g., Daddi et al. 2000). While clustering and voids are evident in Figure 6, there are no obvious $\sim 0.^\circ 5$ structures or gradients in the distribution of EROs in our sample.

5. THE CORRELATION FUNCTION

We determined the angular correlation function using the Landy & Szalay (1993) estimator:

$$\hat{\omega}(\theta) = \frac{DD - 2DR + RR}{RR}, \tag{1}$$

where DD, DR, and RR are the number of galaxy-galaxy, galaxy-random, and random-random pairs at angular separation $\theta \pm \delta\theta/2$. The pair counts were determined in logarithmically spaced bins between $10''$ and $0.^\circ 7$.

We employed the same methodology as Brown et al. (2003) to generate random object catalogs, correct for the integral constraint (Groth & Peebles 1977), and estimate the covariance of the $\hat{\omega}(\theta)$ bins (using the technique of Eisenstein & Zaldarriaga 2001). The random object catalog contains 100 times the number of objects in the ERO catalog, so DR and RR are renormalized accordingly.

The angular correlation function was assumed to be a power law given by

$$\omega(\theta) = \omega(1')\left(\frac{\theta}{1'}\right)^{1-\gamma}, \tag{2}$$

where γ is a constant. This is a good approximation of the observed galaxy spatial correlation function from the 2dFGRS and Sloan Digital Sky Survey (SDSS) on scales of $\lesssim 10\,h^{-1}$ Mpc (Norberg et al. 2001, 2002; Zehavi et al. 2002). Throughout this paper we assume $\gamma = 1.87$, the approximate value of γ for $z < 0.15$ red galaxies from the 2dFGRS and SDSS surveys. For a $\gamma = 1.87$ power law, the integral constraint for this study was approximately 6% of the amplitude of the correlation function at $1'$. Pair counts and the estimate of the angular correlation function (including the integral constraint correction) for $R - K > 5.0$ and 5.5 EROs are presented in Table 3.

The spatial correlation function was obtained using the Limber (1953) equation,

$$\omega(\theta) = \int_0^\infty \frac{dN}{dz}\left\{\int_0^\infty \xi[r(\theta, z, z'), z]\,\frac{dN}{dz'}\,dz'\right\} dz \times \left(\int_0^\infty \frac{dN}{dz}\,dz\right)^{-2}, \tag{3}$$

where dN/dz is the redshift distribution without clustering, ξ is the spatial correlation function, and $r(\theta, z, z')$ is the comoving distance between two objects at redshifts z and z' separated by angle θ on the sky. The spatial correlation function was assumed to be a power law given by

$$\xi(r, z) = [r/r_0(z)]^{-\gamma}. \tag{4}$$

We estimated the redshift distribution for the sample by summing the redshift likelihood distributions of the individual galaxies in each subsample. Model redshift distributions for subsamples selected by apparent magnitude and photometric redshift are shown in Figure 7. While the individual photometric redshifts are not especially accurate, they do include information provided by the observed ERO photometry and are likely to provide a fair approximation of the ERO redshift distribution. Redshift distribution models that only reproduce the apparent ERO number counts and local galaxy luminosity functions (e.g., Daddi et al. 2001; Roche et al. 2002, 2003) have fewer constraints and may have larger systematic errors. The

TABLE 3
THE ANGULAR CORRELATION FUNCTIONS OF $K < 18.40$ EROs FROM 0.98 deg^2 OF THE NDWFS

Color Selection	Angular Scales (deg)	$\omega(\theta)$	DD	$DR \times 10^2 \times N/(N-1)$	$RR \times 10^4 \times N/(N-1)$
$R-K>5.0$.....	0.0028–0.0070	0.631 ± 0.204	88	5515	558532
	0.0070–0.0175	0.282 ± 0.100	424	33602	3346550
	0.0175–0.0440	0.198 ± 0.062	2274	192715	19207198
	0.0440–0.1106	0.069 ± 0.046	12084	1115798	107760586
	0.1106–0.2778	0.018 ± 0.037	60806	5811770	555035500
	0.2778–0.6977	0.018 ± 0.028	244670	23592613	2273794800
$R-K>5.5$.....	0.0028–0.0070	0.722 ± 0.409	20	1193	122608
	0.0070–0.0175	0.064 ± 0.177	80	7502	733626
	0.0175–0.0440	0.240 ± 0.087	510	41951	4199066
	0.0440–0.1106	0.037 ± 0.054	2546	242766	23547906
	0.1106–0.2778	0.018 ± 0.038	13240	1269134	121503332
	0.2778–0.6977	0.020 ± 0.028	53148	5137427	497077474

NOTE.—$N = 671$ and 314 for the $R-K>5.0$ and >5.5, $K < 18.40$ ERO samples, respectively.

estimated median redshift of the $K < 18.40$ EROs is 1.18, which is almost identical to the spectroscopic median redshift of 24 $K_S < 18.7$ EROs from Yan et al. (2004). The median redshift is also similar to $K_S < 18.5$ EROs in the K20 spectroscopic sample (Cimatti et al. 2002; A. Cimatti 2003, private communication).

6. THE CLUSTERING OF EROs

We measured the angular and spatial correlation functions for a series of apparent magnitude, apparent color, absolute magnitude, and redshift bins. A power law of the form $\omega(\theta) = A\theta^{1-\gamma}$ was fitted to the data with γ fixed to 1.87. Much larger imaging surveys, including the completed NDWFS Boötes and Cetus fields, will have sufficient area to accurately measure γ. When parameterizing the power-law fits, we use $\omega(1')$ instead of $\omega(1^\circ)$ because it depends less on the assumed value of γ. Using $\gamma = 1.80$ instead of $\gamma = 1.87$ increases $\omega(1')$ by $\simeq$10% and $\omega(1^\circ)$ by $\simeq$35%. The best-fit values of r_0 do depend on the assumed value of γ, but for the NDWFS ERO sample changing γ from 1.87 to 1.80 increases r_0 by only $\simeq$10%. Measurements of $\omega(1')$ for EROs as a function of K-band limiting magnitude from our study and the literature are summarized in Table 2. Angular correlation functions for apparent magnitude–limited samples are also plotted in Figure 8. Estimates of $\omega(1')$ and r_0 for each of the NDWFS subsamples are presented in Table 4 and discussed in §§ 6.1–6.4.

6.1. *Clustering as a Function of Apparent Magnitude*

The amplitude of the angular correlation function for a series of apparent magnitude–limited samples is presented in Figure 9 and Table 2, along with estimates from the literature. While our $K < 18.4$ sample has a larger volume and more objects than previous studies, our uncertainties are comparable to the published uncertainties of many previous studies. This is due to our inclusion of the covariance when fitting a power law to the data.

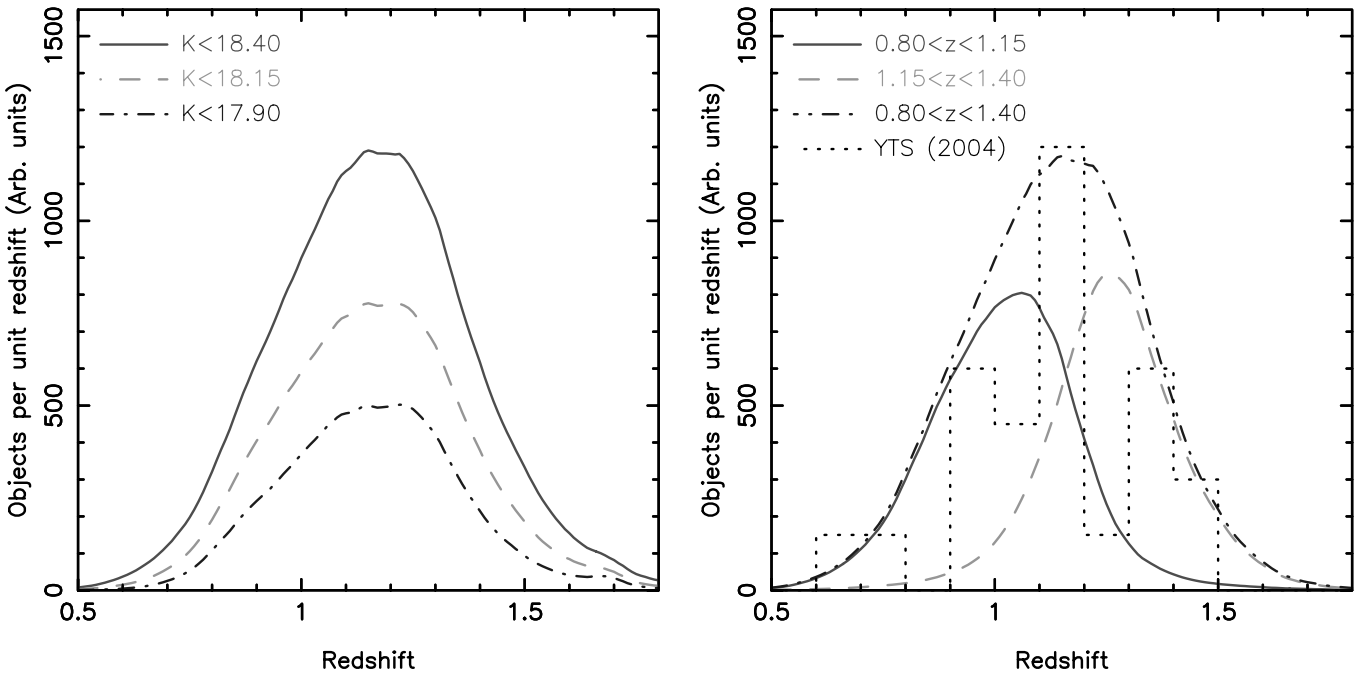

FIG. 7.—Model redshift distributions of NDWFS EROs as a function of apparent magnitude (*left*) and photometric redshift (*right*). The histogram of $K_S < 18.7$ ERO spectroscopic redshifts from Yan et al. (2004) is also shown. Unlike most models of the redshift distribution of $K \gtrsim 19$ EROs (e.g., Daddi et al. 2001; Roche et al. 2002, 2003), the NDWFS $K < 18.40$ ERO redshift distribution model has few objects at $z > 1.5$. [*See the electronic edition of the Journal for a color version of this figure.*]

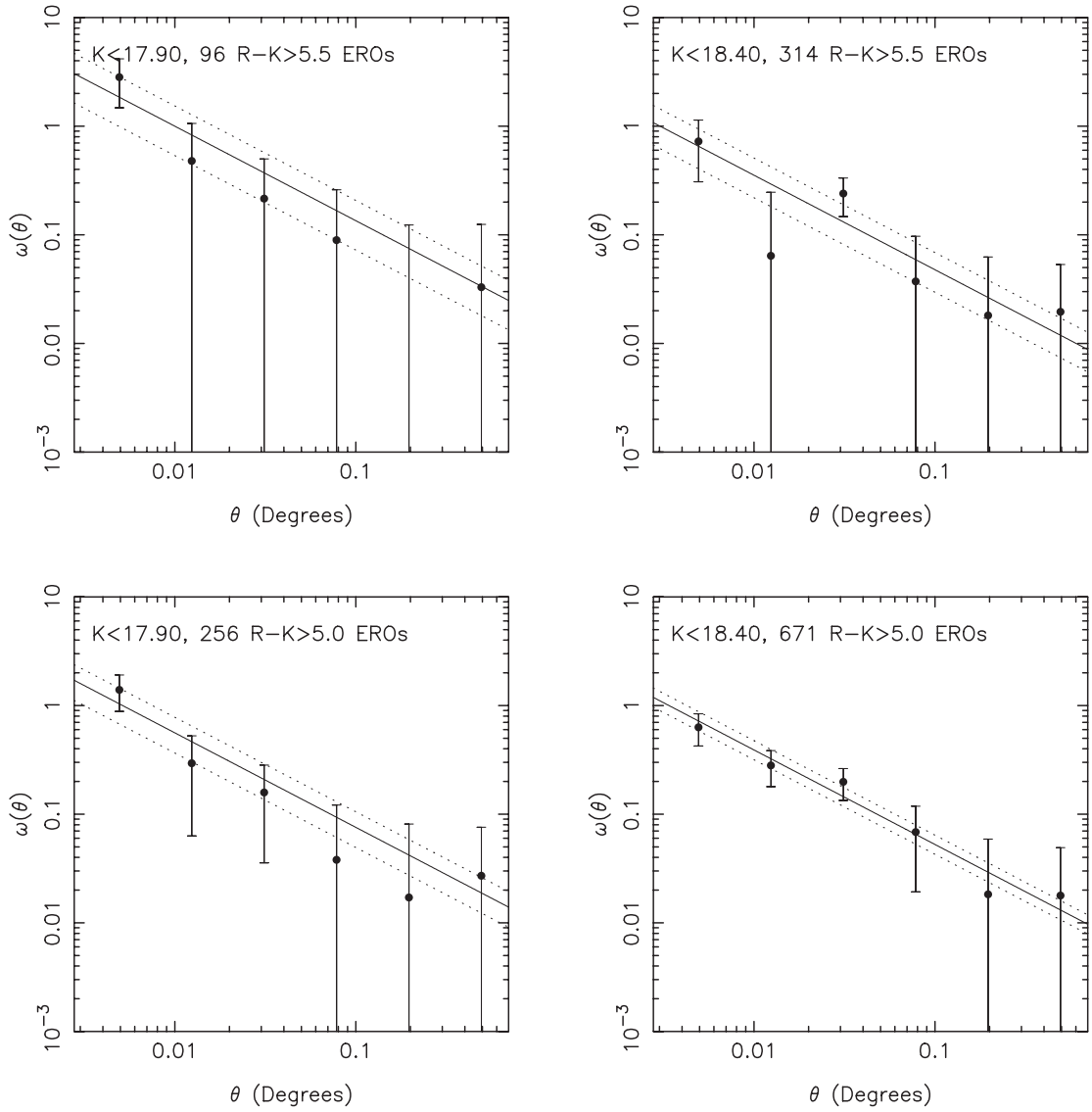

FIG. 8.—Angular correlation function of NDWFS EROs for several apparent K-band magnitude–limited bins. Power-law fits to the data with γ fixed at 1.87 are shown along with ± 1 σ errors (*dotted lines*).

Our estimates of the amplitude of the angular correlation function are ~ 2 σ lower than the smaller $K_S < 18.4$ ERO samples from Daddi et al. (2000). Within our sample we do not see a significant change in the angular clustering amplitude with apparent magnitude, but this is not unexpected because we span a small range of apparent magnitudes.

The first section of Table 4 provides an estimate of r_0 for EROs as a function of apparent limiting magnitude. While the NDWFS r_0 values are accurate to $\sim$15%, each apparent magnitude bin spans a large range of redshift and absolute magnitude. As r_0 is correlated with luminosity in other galaxy samples (e.g., Giavalisco & Dickinson 2001; Norberg et al. 2002; Zehavi et al. 2002; Brown et al. 2003), a correlation between r_0 and apparent magnitude might be expected. We do not observe a significant correlation within the NDWFS, but our uncertainties are too large to rule out such a correlation.

Combining published ERO samples provides spatial clustering measurements over a broad magnitude range. However, it is not possible to directly compare the published r_0 measurements of different ERO samples (Table 1), as different authors use different models of the ERO redshift distribution. Different studies also estimate the uncertainties of the angular correlation function and r_0 using different techniques. In Table 3, we present the NDWFS pair counts for the $R - K > 5.0$ and $R - K > 5.5$, $K < 18.40$ ERO angular correlation functions, so other researchers can apply their techniques for estimating the correlation function to our data. Poisson statistics underestimate the uncertainties of the correlation function on large scales, where object pair counts are high and the uncertainties of the correlation function are dominated by large-scale structure. The uncertainties of clustering measurements from deep pencil beam surveys should be larger than those of the NDWFS, and the large scatter of $K > 19$ ERO clustering measurements shown in Figure 9 may reflect this.

If we assume that the published best-fit values of the amplitude of the angular correlation are correct, then the angular clustering of EROs does decrease with increasing limiting magnitude. We find $\omega(1') = 0.25 \pm 0.05$ for $K < 18.40$ EROs, while Roche et al. (2003) find $\omega(1') \sim 0.13$ for $K < 22$ EROs. Unless the redshift distribution of faint EROs is very broad, the spatial clustering of EROs is decreasing with increasing apparent magnitude. Several studies have measured $r_0 \sim 10\ h^{-1}$ Mpc for faint EROs (Roche et al. 2002, 2003; Daddi et al. 2003; Miyazaki

TABLE 4
THE ANGULAR AND SPATIAL CORRELATION FUNCTIONS OF EROS FROM 0.98 deg^2 OF THE NDWFS

Selection Criterion	Photometric z Range	Absolute Magnitude Range	Apparent Magnitude Range	Number of EROs	$\omega(1')$	Median z	r_0 (h^{-1} Mpc)
			$R - K > 5.0$ EROs Selected by Apparent Magnitude				
$R - K > 5.0$.....	0.80–3.00	$-27.91 < M_K < -24.29$	$15.92 \le K \le 17.90$	256	0.36 ± 0.13	1.17	11.0 ± 2.2
	0.80–3.00	$-27.91 < M_K < -23.95$	$15.92 \le K \le 18.15$	421	0.23 ± 0.07	1.17	9.1 ± 1.5
	0.80–3.00	$-27.91 < M_K < -23.79$	$15.92 \le K \le 18.40$	671	0.25 ± 0.05	1.18	9.7 ± 1.1
			$R - K > 5.5$ EROs Selected by Apparent Magnitude				
$R - K > 5.5$.....	0.80–3.00	$-27.91 < M_K < -24.43$	$15.92 \le K \le 17.90$	96	0.64 ± 0.32	1.22	13.6 ± 3.7
	0.80–3.00	$-27.91 < M_K < -24.25$	$15.92 \le K \le 18.15$	180	0.17 ± 0.13	1.22	7.0 ± 3.1
	0.80–3.00	$-27.91 < M_K < -24.11$	$15.92 \le K \le 18.40$	314	0.23 ± 0.09	1.24	8.6 ± 1.9
			$R - K > 5.0$ EROs Selected by Absolute Magnitude				
$R - K > 5.0$.....	0.80–1.25	$-26.00 < M_K < -25.00$	$16.77 \le K \le 18.40$	108	0.59 ± 0.29	1.16	11.4 ± 3.0
	0.80–1.25	$-25.00 < M_K < -24.50$	$17.35 \le K \le 18.40$	208	0.28 ± 0.12	1.11	9.0 ± 2.1
			$R - K > 5.0$ EROs Selected by Photometric Redshift				
$R - K > 5.0$.....	0.80–1.15	$-26.44 < M_K < -23.79$	$16.28 \le K \le 18.40$	318	0.40 ± 0.10	1.04	10.3 ± 1.4
	1.15–1.40	$-26.69 < M_K < -24.46$	$16.27 \le K \le 18.40$	292	0.35 ± 0.10	1.28	9.2 ± 1.4
	0.80–1.40	$-26.69 < M_K < -23.79$	$16.27 \le K \le 18.40$	610	0.27 ± 0.06	1.15	9.6 ± 1.0

et al. 2003), but their model redshift distributions contain more high-redshift objects than the GOODS $K_S < 20.1$ ERO photometric redshift distribution (Moustakas et al. 2004). If $\omega(1') \simeq 0.13$ for faint EROs and the GOODS photometric redshifts are accurate, then r_0 decreases from $9.7 \pm 1.1\ h^{-1}$ Mpc for $K < 18.40$ to $r_0 \sim 7.5\ h^{-1}$ Mpc for $K \gtrsim 20$ EROs. Red galaxies at $z < 1$ have a comparable range of r_0 values (e.g., Norberg et al. 2002; Zehavi et al. 2002; Brown et al. 2003), and their spatial clustering is correlated with absolute magnitude. The current measurements of ERO clustering are consistent with EROs being the progenitors of local red galaxies.

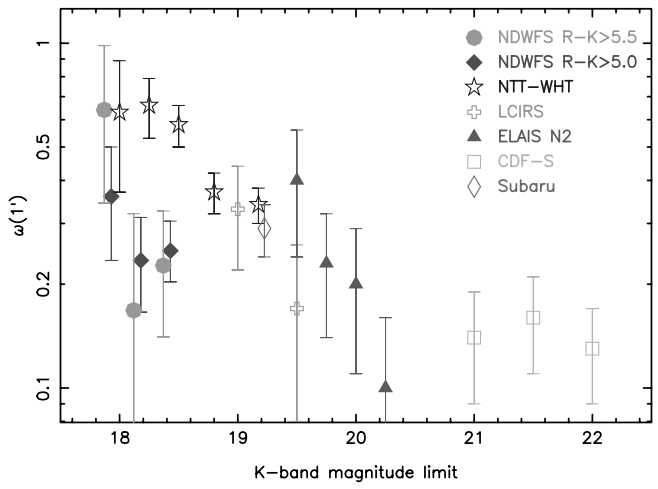

FIG. 9.—Amplitude of the ERO angular correlation function at 1′ as a function of K-band limiting magnitude. The error bars show the published uncertainties, which may not include the contribution of the covariance. The 4 arcmin^2 HDF-S measurement of $K < 24$ ERO clustering (not shown) is $\omega(1') = 0.16 \pm 0.10$. Combining the NDWFS with previous ERO clustering studies, there is evidence for the ERO angular clustering decreasing with increasing magnitude. Unless the redshift distribution of $K > 19$ EROs is much broader than the redshift distribution of $K < 19$ EROs, the spatial clustering of faint EROs is somewhat weaker than the spatial clustering of $K < 19$ EROs. [*See the electronic edition of the Journal for a color version of this figure.*]

6.2. *Clustering as a Function of Apparent Color*

We present the clustering of $R - K > 5.0$ and 5.5 EROs in Figure 9 and Table 4. We find that the angular and spatial clustering of $R - K > 5.5$ galaxies does not differ significantly from the remainder of the sample. Low-redshift galaxies may have a bimodal distribution of clustering properties as a function of color (Budavári et al. 2003). This could be due to the bimodal distribution of galaxy colors at low redshift, or a bimodality of the clustering properties of galaxies as a function of star formation rate. If the clustering is bimodal at all redshifts, we would not expect a correlation between clustering and color within a red galaxy sample. We do not see a correlation of clustering with color, but a larger sample with improved photometric redshifts is required so that accurate spatial clustering measurements can be performed as a function of rest-frame color.

6.3. *Clustering as a Function of Absolute Magnitude*

The clustering of EROs as a function of absolute magnitude is presented in Table 4. We have determined the absolute magnitudes (without evolution corrections) of the EROs using the best-fit τ-model SED. As shown in Figure 2, ERO photometric redshifts can have large uncertainties and our ERO absolute magnitudes are, at best, approximations. The two absolute magnitude bins are approximately volume limited samples with the same photometric redshift range. Both absolute magnitude bins are extremely luminous and contain EROs approximately 4 times brighter than the local value of L^* ($M_K^* = -23.44 \pm 0.03$; Cole et al. 2001). We do not see a significant correlation between luminosity and r_0 within the sample. The correlation between galaxy luminosity and clustering is seen unambiguously only in $z < 1$ samples (e.g., 2dFGRS and SDSS), which contain a factor of $\gtrsim$10 more galaxies than the NDWFS ERO sample. A strong correlation between ERO luminosity and spatial clustering remains plausible and may be detected with an analysis of the complete NDWFS.

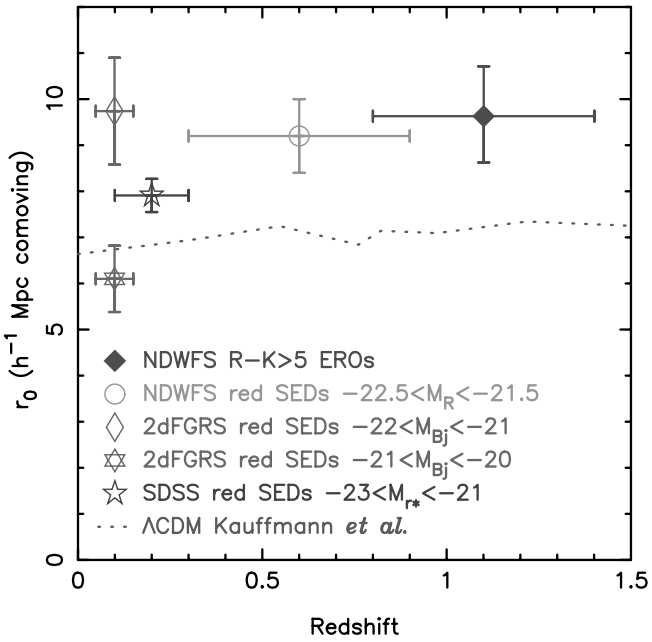

FIG. 10.—Spatial correlation function of the most luminous red galaxies as a function of redshift. The NDWFS ERO data points are shown along with previous r_0 measurements of $z < 1$ red galaxies from the 2dFGRS, SDSS, and NDWFS (Norberg et al. 2002; Budavári et al. 2003; Brown et al. 2003). If $K < 18.40$ EROs are the progenitors of local $\sim 4L^*$ early-type galaxies, the data are consistent with little or no evolution of r_0 for $z < 1.4$ red galaxies. A ΛCDM model for the clustering of early-type galaxies selected by stellar mass (Kauffmann et al. 1999) also exhibits little evolution but has lower clustering than most of the samples plotted here. [*See the electronic edition of the Journal for a color version of this figure.*]

6.4. *Clustering as a Function of Redshift*

We measured the clustering of EROs within the sample with two photometric redshift bins, $0.80 < z < 1.15$ and $1.15 < z < 1.40$. We exclude EROs beyond these redshift ranges, since they contribute less than 10% of the total $K < 18.40$ ERO number counts. The results are presented in Table 4 and Figure 10. We do not observe significant evolution of r_0 with redshift within the ERO sample. However, our uncertainties are large and the redshift distributions of the two samples overlap, so they are not entirely independent.

7. DISCUSSION

The clustering of $0.80 < z < 1.40$, $K < 18.40$ EROs is well approximated by a power law with $r_0 = 9.6 \pm 1.0\ h^{-1}$ Mpc and γ fixed at 1.87. As EROs are thought to be the progenitors of local elliptical galaxies, it is useful to compare the clustering measurements of these populations. In the 2dFGRS, the spatial correlation function increases from $r_0 = 6.10 \pm 0.72\ h^{-1}$ Mpc for $\simeq 2L^*$ red galaxies to $r_0 = 9.74 \pm 1.16\ h^{-1}$ Mpc for $\simeq 4L^*$ red galaxies (Norberg et al. 2002). Other $z < 1$ surveys, including the NDWFS, measure comparable spatial clustering for red galaxies (e.g., Willmer et al. 1998; Budavári et al. 2003; Brown et al. 2003). It is not unreasonable to assume that the brightest EROs are the progenitors of the $\simeq 4L^*$ red galaxies in the local universe, since the comoving spatial clustering of the two populations is comparable. However, this assumes that models predicting little or no evolution of the $\gtrsim L^*$ galaxy correlation function (e.g., Kauffmann et al. 1999; Benson et al. 2001) are valid.

If $K < 18.40$ EROs are the progenitors of the most luminous local red galaxies, fainter EROs could the progenitors of $\sim L^*$ red galaxies. Several previous studies of fainter EROs find that they are very strongly clustered, with $r_0 \sim 10\ h^{-1}$ Mpc (Roche et al. 2002, 2003; Daddi et al. 2003; Miyazaki et al. 2003). This is much stronger than the clustering of local L^* red galaxies, where $r_0 \simeq 6\ h^{-1}$ Mpc (Norberg et al. 2002; Zehavi et al. 2002). However, the ERO spatial clustering measurements could be subject to large, and possibly systematic, errors. Several of these measurements use model redshift distributions that are primarily constrained by the local galaxy luminosity function and faint galaxy number counts (Daddi et al. 2001; Roche et al. 2002, 2003). Other model redshift distributions use unverified photometric redshifts (Miyazaki et al. 2003) or photometric redshifts that could only be verified with galaxies other than EROs (Firth et al. 2002). As shown in Figure 9, the angular clustering of EROs does decrease with increasing apparent magnitude. Unless the redshift distribution of $K \gtrsim 20$ EROs is very broad, the spatial clustering of $K \gtrsim 20$ EROs is weaker than the spatial clustering of $K < 18.40$ EROs.

While $K < 18.40$ EROs may be the progenitors of most luminous local elliptical galaxies, our spatial clustering measurement should be treated with some caution. Our ERO sample spans broad ranges of redshift and absolute magnitude ($-27.9 \lesssim M_K - 5 \log h \lesssim -23.9$). The luminosity and density evolution of EROs and red galaxies at $z < 1$ has not been accurately determined. The PEGASE τ-models predict ~ 0.8 mag of luminosity evolution at $z < 1$, so EROs would be the progenitors to $\simeq 2L^*$ red galaxies. If this were the case, the spatial correlation function would be decreasing with decreasing redshift, which is unphysical. The uncertain luminosity and density evolution of EROs limits the use of $>L^*$ EROs to measure the evolution of the galaxy spatial correlation function.

Current ERO spatial clustering measurements, including our study, have large uncertainties and may be subject to systematic errors. We will significantly reduce the random uncertainties of ERO clustering measurements when we analyze the entire NDWFS Boötes field. The uncertainties and systematic errors of our photometric redshifts will be accurately determined as we obtain more spectroscopic redshifts. We will also improve the photometric redshifts for EROs by using NDWFS, FLAMINGOS (Gonzalez et al. 2004), and *Spitzer Space Telescope* data. We will then be able to accurately measure the spatial clustering of EROs as a function of luminosity, color, and redshift.

8. SUMMARY

We have measured the clustering of 671 $K < 18.40$ EROs with a 0.98 deg^2 subset of the NDWFS. This study covers an area nearly 5 times larger and has twice the sample size of any previous ERO clustering study. The angular clustering of $K < 18.40$, $R - K > 5.0$ EROs is well described by a power law with $\omega(1') = 0.25 \pm 0.05$ and $\gamma = 1.87$. Using a model of the ERO redshift distribution derived from photometric redshifts, we find that the spatial clustering of $K < 18.40$ EROs is given by $r_0 = 9.7 \pm 1.0\ h^{-1}$ Mpc comoving. Within our study, we detect no significant correlations between ERO clustering and apparent magnitude, apparent color, absolute magnitude, or redshift. However, our uncertainties are large and such correlations may exist. When combined with data from other studies, there is evidence of the angular clustering of EROs decreasing with increasing apparent magnitude. Unless the redshift distribution of $K \gtrsim 20$ EROs is very broad, the spatial clustering of EROs decreases with increasing apparent magnitude. As the uncertainties and systematic errors of current ERO spatial clustering

measurements are large, they do not yet provide strong tests of models of structure evolution and galaxy formation.

This research was supported by the National Optical Astronomy Observatory, which is operated by the Association of Universities for Research in Astronomy (AURA), Inc., under a cooperative agreement with the National Science Foundation. We thank our colleagues on the NDWFS team and the KPNO and CTIO observing support staff. We are grateful to Frank Valdes, Lindsey Davis, and the IRAF team for the packages used to reduce the imaging data. We thank Alyson Ford, Chris Greer, Heather Gross, Lissa Miller, and Erin Ryan for helping reduce KPNO Mosaic-1 and ONIS imaging data used for our work. While working on this paper, the authors had many useful discussions about galaxy clustering with Tod Lauer and Daniel Eisenstein.

REFERENCES

Alexander, D. M., Vignali, C., Bauer, F. E., Brandt, W. N., Hornschemeier, A. E., Garmire, G. P., & Schneider, D. P. 2002, AJ, 123, 1149
Benson, A. J., Frenk, C. S., Baugh, C. M., Cole, S., & Lacey, C. G. 2001, MNRAS, 327, 1041
Bertin, E., & Arnouts, S. 1996, A&AS, 117, 393
Brown, M. J. I., Dey, A., Jannuzi, B. T., Lauer, T. R., Tiede, G. P., & Mikles, V. J. 2003, ApJ, 597, 225
Budavári, T., et al. 2003, ApJ, 595, 59
Cimatti, A., et al. 2002, A&A, 381, L68
Cole, S., et al. 2001, MNRAS, 326, 255
Daddi, E., Broadhurst, T., Zamorani, G., Cimatti, A., Röttgering, H., & Renzini, A. 2001, A&A, 376, 825
Daddi, E., Cimatti, A., Pozzetti, L., Hoekstra, H., Röttgering, H. J. A., Renzini, A., Zamorani, G., & Mannucci, F. 2000, A&A, 361, 535
Daddi, E., et al. 2002, A&A, 384, L1
———. 2003, ApJ, 588, 50
Devriendt, J. E. G., Guiderdoni, B., & Sadat, R. 1999, A&A, 350, 381
Dey, A., Graham, J. R., Ivison, R. J., Smail, I., Wright, G. S., & Liu, M. C. 1999, ApJ, 519, 610
Dey, A., Spinrad, H., & Dickinson, M. 1995, ApJ, 440, 515
Donas, J., Milliard, B., & Laget, M. 1995, A&A, 303, 661
Efstathiou, G., Bernstein, G., Tyson, J. A., Katz, N., & Guhathakurta, P. 1991, ApJ, 380, L47
Eisenstein, D. J., & Zaldarriaga, M. 2001, ApJ, 546, 2
Elston, R., Rieke, G. H., & Rieke, M. J. 1988, ApJ, 331, L77
Falco, E. E., et al. 1999, ApJ, 523, 617
Fioc, M., & Rocca-Volmerange, B. 1997, A&A, 326, 950
Firth, A. E., et al. 2002, MNRAS, 332, 617
Giavalisco, M., & Dickinson, M. 2001, ApJ, 550, 177
Gonzalez, A., et al. 2004, AAS Meeting, 204, 48.07
Groth, E. J., & Peebles, P. J. E. 1977, ApJ, 217, 385
Hu, E. M., & Ridgway, S. E. 1994, AJ, 107, 1303
Jannuzi, B. T., & Dey, A. 1999, in ASP Conf. Ser. 191, Photometric Redshifts and High Redshift Galaxies, ed. R. J. Weymann et al. (San Francisco: ASP), 111
Kauffmann, G., Colberg, J. M., Diaferio, A., & White, S. D. 1999, MNRAS, 307, 529
Kron, R. G., 1980, ApJS, 43, 305
Landy, S. D., & Szalay, A. S. 1993, ApJ, 412, 64
Limber, N. D. 1953, ApJ, 117, 134
Madgwick, D. S., et al. 2002, MNRAS, 333, 133
Malmquist, K. G. 1920, Medd. Lund Ser. II, 22, 1
McCarthy, P. J., Persson, S. E., & West, S. C. 1992, ApJ, 386, 52
Miyazaki, M., et al. 2003, PASJ, 55, 1079
Mobasher, B., et al. 2004, ApJ, 600, L167
Moriondo, G., Cimatti, A., & Daddi, E. 2000, A&A, 364, 26
Moustakas, L. A., et al. 2004, ApJ, 600, L131
Norberg, P., et al. 2001, MNRAS, 328, 64
———. 2002, MNRAS, 332, 827
Roche, N. D., Almaini, O., Dunlop, J., Ivison, R. J., & Willott, C. J. 2002, MNRAS, 337, 1282
Roche, N. D., Dunlop, J., & Almaini, O. 2003, MNRAS, 346, 803
Somerville, R. S., Lee, K., Ferguson, H. C., Gardner, J. P., Moustakas, L. A., & Giavalisco, M. 2004, ApJ, 600, L171
Somerville, R. S., Lemson, G., Sigad, Y., Dekel, A., Kauffmann, G., & White, S. D. M. 2001, MNRAS, 320, 289
Spinrad, H., Dey, A., Stern, D., Dunlop, J., Peacock, J., Jimenez, R., & Windhorst, R. 1997, ApJ, 484, 581
Stiavelli, M., & Treu, T. 2001, in ASP Conf. Ser. 230, Galaxy Disks and Disk Galaxies, ed. J. G. Funes & E. M. Corsini (San Francisco: ASP), 603
Willmer, C. N. A., da Costa, L. N., & Pellegrini, P. S. 1998, AJ, 115, 869
Yan, L., Thompson, D., & Soifer, B. T. 2004, AJ, 127, 1274
Zehavi, I., et al. 2002, ApJ, 571, 172